PHYSICAL SCIENCES

A flexible electronic strain sensor for the real-time monitoring of tumor regression

Alex Abramson[1]†, Carmel T. Chan[2,3], Yasser Khan[1]‡, Alana Mermin-Bunnell[1,4], Naoji Matsuhisa[1]§, Robyn Fong[5], Rohan Shad[5], William Hiesinger[5], Parag Mallick[2,6], Sanjiv Sam Gambhir[2,3,4,6,7]||, Zhenan Bao[1]*

Copyright © 2022 The Authors, some rights reserved; exclusive licensee American Association for the Advancement of Science. No claim to original U.S. Government Works. Distributed under a Creative Commons Attribution NonCommercial License 4.0 (CC BY-NC).

Assessing the efficacy of cancer therapeutics in mouse models is a critical step in treatment development. However, low-resolution measurement tools and small sample sizes make determining drug efficacy in vivo a difficult and time-intensive task. Here, we present a commercially scalable wearable electronic strain sensor that automates the in vivo testing of cancer therapeutics by continuously monitoring the micrometer-scale progression or regression of subcutaneously implanted tumors at the minute time scale. In two in vivo cancer mouse models, our sensor discerned differences in tumor volume dynamics between drug- and vehicle-treated tumors within 5 hours following therapy initiation. These short-term regression measurements were validated through histology, and caliper and bioluminescence measurements taken over weeklong treatment periods demonstrated the correlation with longer-term treatment response. We anticipate that real-time tumor regression datasets could help expedite and automate the process of screening cancer therapies in vivo.

INTRODUCTION

In the process of clinical translation, thousands of potential cancer drugs are tested for every one drug that makes it to patients. Oncology researchers use a suite of in vitro high-throughput screening models that implement computational algorithms, genomics testing, cell culture, and organoid systems to assess the efficacy of these numerous drugs quickly and inexpensively against a given cancer type (*1*–*4*). In vivo models, however, generally produce results that more closely resemble clinical outcomes (*5*). Researchers typically read out in vivo models by comparing tumor volume regression between multiple replicates of treated and untreated controls. However, inherent biological variations combined with low-resolution measurement tools and small sample sizes make determining drug efficacy in vivo a difficult, labor-intensive task (*6*). Accurately determining treatment response is critical to clinical translation, and tools automating in vivo tumor regression measurements could facilitate this process by gathering high-resolution continuous datasets in larger animal cohorts. Such advances in data quality and labor reduction could lead to automated high-throughput in vivo drug testing setups and more accurate experimental results.

Here, we present an elastomeric-electronic tumor volume sensor capable of autonomously reading out cancer treatment efficacy studies in vivo. Using advances in flexible electronic materials (*7*–*12*), we designed a conformal, wearable strain sensor that continuously measures, records, and broadcasts tumor volume changes occurring in subcutaneously implanted tumors on the minute time scale. The sensor's real-time dataset enables us to track the immediate pharmacodynamic response of a given drug by recording significant tumor shrinkage continuously. In two unique tumor models, our sensor was able to discern differences in tumor volume dynamics between drug- and vehicle-treated tumors within hours following therapy initiation in vivo. Short-term regression measurements in these models were validated by histology taken within hours following therapy initiation, and caliper and bioluminescence measurements over weeklong treatment periods demonstrated correlation with longer-term treatment response.

This sensor achieves three main advances over other common tumor measurement tools such as calipers, implantable pressure sensors, and imagers. First, because the sensor remains in place over the entire measurement period and takes measurements every 5 min, it is possible to generate a four-dimensional (4D), time-dependent dataset that eliminates the need for any guesswork on measurement timing. Imaging techniques such as computed tomography (CT) and bioluminescence are unable to achieve these same time resolutions over long measurement periods. This is due to the toxicity limitations associated with the necessary radiation and contrast dye in CT imaging; in addition, high-resource and cost constraints prevent imaging scale up to larger cohorts or more frequent sampling time points (*13*). Moreover, implantable pressure sensors require invasive procedures that compromise the mechanical integrity of the tumor, and they work best when measuring tumors encapsulated within a solid environment such as bone (*14*). Second, the strain sensor has the capability of precisely distinguishing size changes that are difficult to detect using caliper and bioluminescence imaging measurements. This is due to the errors associated with the physical measurement of soft tissue (*15*–*17*) and the positive but inexact correlation between bioluminescence readouts and tumor volume (*18*), respectively. Third, the sensor is entirely autonomous and noninvasive. Thus, using it reduces the costs and labor associated with performing measurements and enables direct data comparisons between operators. Consequently, it enables fast, inexpensive,

[1]Department of Chemical Engineering, Stanford University, Stanford, CA 94305, USA. [2]Department of Radiology, Stanford University, Stanford, CA 94305, USA. [3]Molecular Imaging Program at Stanford (MIPS) and Bio-X Program, Stanford University, Stanford CA, 94305, USA. [4]Department of Bioengineering, Stanford University, Stanford, CA 94305, USA. [5]Department of Cardiothoracic Surgery, Stanford University School of Medicine, Stanford, CA 94305, USA. [6]Canary Center at Stanford for Cancer Early Detection, Stanford University, Stanford, CA 94305, USA. [7]Department of Medicine, Stanford University, Stanford, CA 94305, USA.
*Corresponding author. Email: zbao@stanford.edu
†Present address: School of Chemical and Biomolecular Engineering, Georgia Institute of Technology, Atlanta, GA, 30318, USA.
‡Present address: Department of Electrical and Computer Engineering, University of Southern California, Los Angeles, CA, USA.
§Present address: Institute of Industrial Science, The University of Tokyo, Tokyo, Japan.
||Deceased.

large-scale preclinical drug discovery testing setups. Moreover, the continuous and highly sensitive measurements generated by our sensor enable the recording of immediate tumor volume regression following treatment initiation rather than the more general growth trends captured using other methods. Experimental implantable microdevices in development have also been shown to enable rapid testing of therapeutics in vivo, but these tools require invasive procedures and biopsy sampling, and they do not capture the full pharmacokinetics and pharmacodynamics of drug delivery (*19*). Furthermore, sensor arrays have been developed, which generate 2D maps of tissue moduli, but these sensors are designed to detect biomechanical property differences on 2D surfaces rather than determine volumetric changes on 3D objects (*20*, *21*). We call our technology FAST, which stands for flexible autonomous sensors measuring tumor volume regression.

RESULTS

Designing a strain sensor for measuring tumor volume progression or regression

Our wireless FAST technology for real-time monitoring of tumor size progression or regression can be applied to tumors on or near the skin (Fig. 1, A to D). The sensor, which is wrapped around the tumor, measures the change in the tumor's circumference over time. Similar to caliper tumor volume measurements, the tumor circumference measurement is a function of two of the three characteristic diameters of the tumor. The two measurements are directly proportional to each other; however, because the circumference is a longer length than the diameter, it is less susceptible to measurement error. Using a soft, fixed sensor to measure a soft tissue also reduces the error associated with tumor volume measurements, as calipers measure different lengths on soft tissues depending on the pressure applied by the user. Moreover, because the sensor remains wrapped around the tumor for the duration of the study, it readily generates high-resolution rate-of-change datasets on tumor progression or regression.

The FAST sensor is fabricated by depositing a 50-nm layer of gold on top of a drop-casted layer of styrene-ethylene-butylene-styrene (SEBS), and it can be easily scaled up for mass manufacturing (see Supplementary Text and fig. S1). Because the sensor is fully flexible and stretchable, it readily expands or shrinks with the tumor as it progresses. Compared to other homogenous sensors where readouts increase linearly with strain, the resistance in this sensor rises exponentially as strain grows, as explained through percolation theory; when strain is applied, microcracks in the gold layer lose contact with each other, increasing the tortuosity of the electron path length through the sensor (Fig. 1B). The relative change in resistance in the sensor spans two orders of magnitude as it is stretched from 0 to 75% strain and can detect changes down to a 10-μm scale resolution (Fig. 1, E and F). At 100% strain, the electrical connection between the two ends of the sensor breaks; however, the sensor can stretch to over 200% strain before the SEBS ruptures (see fig. S2), and it is able to regain an electrical connection when the sensor returns to a lower strain. By changing the thickness of the SEBS layer (Fig. 1G and fig. S2), it is possible to increase the stress that can be applied to the sensor before it ruptures.

A custom-designed printed circuit board (PCB) and a cell phone app enable live and historical sensor readouts with the press of a button (Fig. 1, C and D, and fig. S3). To read out the sensor, it is placed in series with a known resistor on the board, and a known voltage is applied across the circuit. The voltage drop over the known resistor is amplified by an instrumentation amplifier, converted to a digital signal, and read out by an analog-to-digital converter of a microcontroller. To read out resistances between 300 and 60,000 ohms accurately and precisely, the circuit board applies three different voltage biases through the resistive sensor and chooses the most accurate reading depending on the sensor's resistance. We measured the error in sensor readout to be 1 to 2%, as calculated through in vitro measurements of known resistors (see fig S3). In vivo, the sensor measurements had a 12% error when assessing the same tumor ($n = 27$ tumors, three to four measurements per tumor). This error was due to slight movements by the mice. To mitigate this error, we programmed our sensor to take 32 consecutive measurements for each 5-min data point; this translates to a standard measurement error of 2%, approximately equal to the error associated with the sensor electronics readout system. To further reduce the error, we recorded the median measurement rather than the mean to eliminate the effects of outlier data points from large movements and plot a seven-point moving average in our reported figures. The assembled device can continuously read out measurements every 5 min for >24 hours on a 150-mA·hour battery. Further optimization of the machine code would increase the battery life closer to the theoretical maximum of measurements once per hour for >10 days.

We designed a 3D printed housing mechanism for FAST to ensure that the sensor and PCB fit comfortably on the mouse and accurately record tumor volume progression or regression (Fig. 1D and fig. S1). The housing has a flexible base capable of conforming to the mouse's skin and rigid rods that ensure that the ends of the sensors remain fixed in place. The rigid PCB and battery are placed on the flexible backpack above the skin so that the rigid materials do not affect the conformal contact of the device on the skin (Fig. 1H). Fixing the ends of the sensors to rigid components, rather than placing them directly on flexible skin, allows us to calculate the sensor's change in strain attributed to tumor growth without the additional convoluting factor of skin displacement. The sensors themselves are prestretched up to 50%, enabling us to accurately read out both growth and shrinkage events of up to 3× tumor volume change within the device's most sensitive strain range of 25 to 75%. To characterize the assembled device's ability to discern volume variations in shapes in vitro, we measured the sensor's output when placed on top of the 3D printed model tumors (Fig. 1I). The sensors recorded significant changes in readouts for objects as small as 65 mm^3 in volume and as large as 750 mm^3 in volume. Because of 3D printing resolution limits, the smallest diameter change tested was Δ0.4 mm (Δ7.7%). Changing the initial strain on the sensor allows for the measurement of larger objects as well. When tested on tumors in vivo, FAST sensor resistance readouts correlated closely to tumor volume measurements ascertained via calipers (Fig. 1J). The correlation between bioluminescence measurements and caliper tumor volume measurements is provided in Fig. 1K as a comparison. We provide a method for converting the three characteristic circumferences of a tumor, as measured by the FAST sensor, into a measurement of the tumor's volume in the Supplementary Materials. With an established correlation between single measurement FAST sensor readouts and tumor volume measurements, we next assessed continous FAST sensor readouts in vivo.

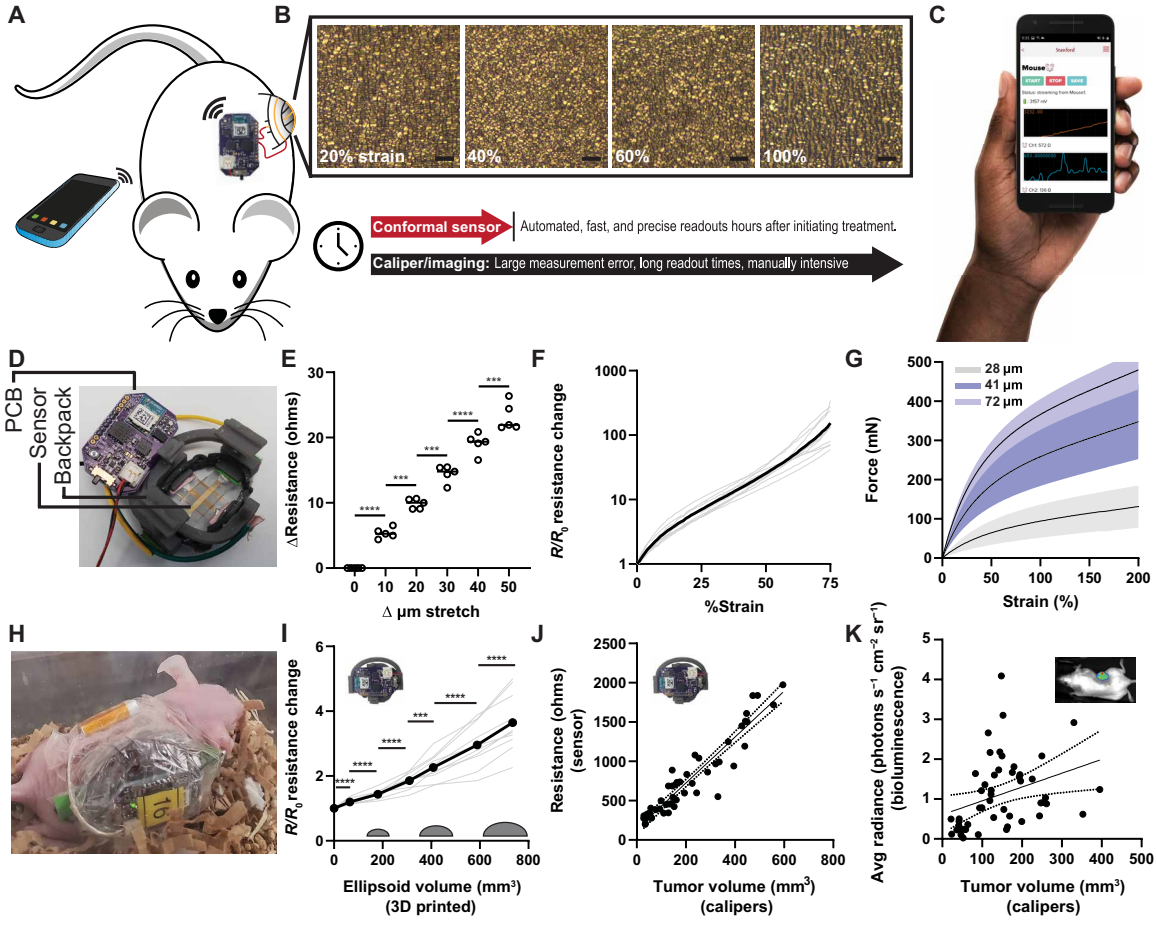

Fig. 1. Flexible autonomous sensors measuring tumor volume regression. (**A**) FAST technology. (**B**) Light microscopy of cracked gold strain sensor at varying strains. Scale bars, 20 μm. (**C**) An app recording the resistance change in sensor. (**D**) FAST contains a printed circuit board (PCB), stretchable strain sensors, and a backpack to hold the sensor on the mouse. (**E**) Resistance changes in sensors when stretched in 10-μm increments from a prestrain of 50% [individual points from five sensors; line, median; one-way analysis of variance (ANOVA) with Tukey's multiple comparisons test]. (**F**) Fold change in resistance of strained sensors (individual curves from 10 sensors; bold line, average). (**G**) Force required to strain sensors of varying SEBS substrate thicknesses (individual curves from 12 to 13 sensors; line, average ± SD). (**H**) FAST backpack on mouse held in place using Tegaderm. (**I**) Fold change in resistance of FAST measuring 3D printed ellipsoids comparable to tumors (individual curves from 10 sensors; bold line, average; ratio paired *t* test). (**J** and **K**) Caliper measured in vivo tumor volumes correlate with (J) FAST resistance outputs and (K) bioluminescence average radiance values [(J) 50 points, three FAST sensors (10 to 20 measurements per sensor) and (K) 50 points, one imaging system; lines, best fit linear regressions ±95% confidence interval]. See fig. S4 for further characterization. ***$P < 0.001$, ****$P < 0.0001$. Photo credits: Alex Abramson (C, D, and H) and Facebook Design Resources (C).

Continuously tracking tumor regression in vivo

In vivo testing in two cancer models demonstrated that FAST detected statistically significant variations in the dynamics of tumor growth and shrinkage within 5 hours after treatment initiation when comparing mice dosed with drug or vehicle alone. These short-term variations in tumor volume dynamics correlated with longer-term treatment efficacy readouts performed by the sensor, calipers, and bioluminescence imaging. To generate the first animal model, we subcutaneously implanted Nu/Nu mice with bioluminescent HCC827 human lung cancer cells that had sensitivity to erlotinib (*22*). Erlotinib is an orally dosed small-molecule drug that targets the epidermal growth factor receptor (EGFR); its pharmacokinetics and pharmacodynamics occur on the time scale of hours (*22*–*24*). Tegaderm and tissue glue were used to fix the sensor, battery, and holder on the mice. In our studies, we demonstrated that this wrapping protocol holds the sensors in place on the mice for at least 1 week. In our studies, we tested the sensor as both a continuous, wearable device and as a single application readout device. Furthermore, we compared the ability for our sensor to read out tumor volume progression or regression with a caliper and a luminescence imaging system.

We initially began characterizing our sensor by testing it on growing untreated tumors. Eight days after tumor inoculation, when the tumor volumes were approximately 100 mm^3, our sensor detected tumor growth over a 12-hour period by reading out an increase in resistance by a range of +21 to +64 ohms, with an average increase of 4.3 ± 2.2 ohms/hour (mean ± SD; $n = 6$) (Fig. 2A). This increasing resistance readout directly correlated with increasing tumor size. As a comparison to other measurement methods, over a 7-day period, the tumor circumferences grew approximately 5.5 mm, and the tumor volume grew an average of 50 mm^3 as measured via calipers; this corresponds to an average growth in tumor circumference of 400 μm, an average growth in tumor volumes of 3.6 mm^3, and an average measured increase in sensor length of 130 μm every 12-hour period (see the Supplementary Materials for calculation to convert change in circumference to change in sensor length). The relationship

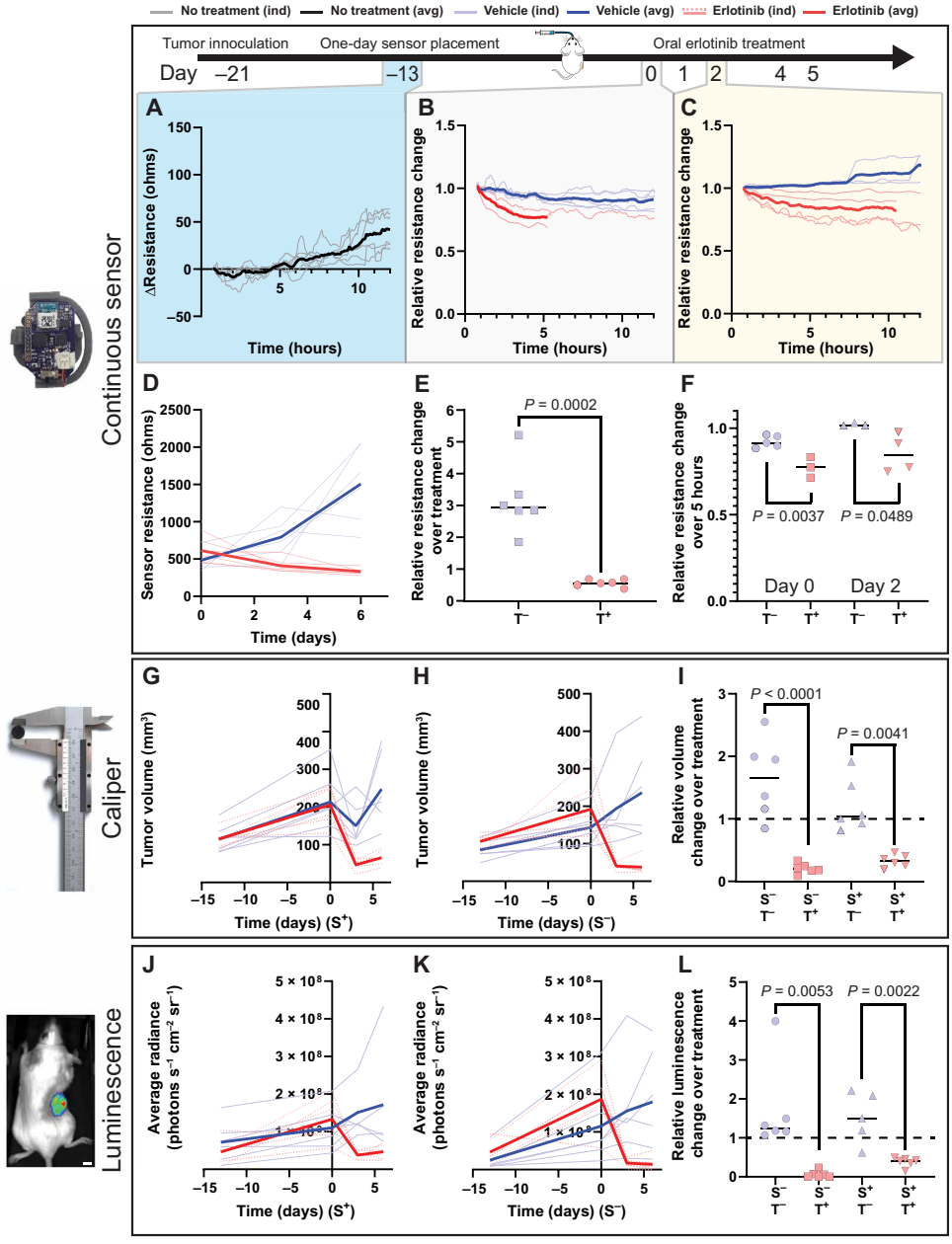

Fig. 2. FAST sensor detects a decrease in tumor volume sooner than existing methods in HCC827 mouse models treated orally with erlotinib. (**A** to **C**) FAST reads out tumor volume progression or regression continuously at 5-min intervals in (A) Nu/Nu mice with ~100-mm^3 subcutaneous HCC827 human lung cancer tumors receiving no treatment and (B and C) mice with ~200-mm^3 tumors receiving erlotinib (50 mg/kg) or vehicle treatments at intervals described in the figure. Individual mouse sensor trend lines are presented as seven-point moving averages. (**D**) FAST sensor measurements over the entire treatment period. (**E** and **F**) Erlotinib- and vehicle-treated mice demonstrate significantly different sensor readouts over (E) the entire treatment period and (F) just 5 hours after treatment administration. (**G** to **I**) Caliper and (**J** to **L**) luminescence imaging confirm the tumor volume measurements recorded by FAST and demonstrate that wearing the FAST device does not affect the outcomes of the treatment experiments. S^+, with FAST sensor; S^-, no FAST sensor; T^+, erlotinib treatment; T^-, vehicle treatment; data are presented as individual data points or curves; bold, average; unpaired two-tailed Student's *t* tests. Scale bar, 5 mm.

between measured resistance changes and measured sensor length changes of 4 ohms/10-μm sensor stretch on in vivo tumors closely correlate to the in vitro measurements provided in Fig. 1E. We further characterized the relationship among the sensor, the caliper, and the bioluminescence measurements by ranking the readouts of each device according to magnitude (see fig. S4). After ranking measurement magnitudes three times over a 7-day period, the sensor and caliper measurements showed the closest correlation with an average rank difference of 1.59. The sensor and luminescence imager recorded an average rank difference of 1.74. Last, the caliper and luminescence imager exhibited an average rank difference of 1.77. These data demonstrate that the FAST sensor measurements of tumor circumference correlate well with other common measurement systems.

To evaluate the ability for FAST to measure biologically significant changes in tumor volumes in vivo during erlotinib treatment, we performed experiments controlling for the pharmacodynamic effects of the treatment and the mechanical effects of the sensor backpack. This required separating the mice into four groups to control for both the sensor and the treatment. FAST, caliper, and luminescence imaging measurements conveyed tumor shrinkage in all erlotinib-treated mice throughout the 6-day treatment period. These same measurement techniques also reported tumor growth in vehicle-treated mice throughout the same period (Fig. 2). These trends were recorded irrespective of the presence of the FAST sensor. The FAST sensor, however, began detecting a change in tumor regression or progression almost immediately following therapy administration, compared to the other measurement techniques that required several days to discern a biologically significant difference. Within 5 hours of placing the sensors on the mice, all vehicle-treated mice demonstrated larger relative sensor readouts compared to the erlotinib-treated mice ($P = 0.0037$; Fig. 2B); this occurred again on a following dosage day as well ($P = 0.0489$; Fig. 2C). When bioluminescence imaging or caliper measurements were used at the 5-hour time point, no statistical significance was found between the treated and untreated groups (bioluminescence, $P = 0.3173$; caliper, $P = 0.3953$). This may have been due to the large measurement error associated with these measurement tools or biologic variability (see fig. S5); because of these measurement and biologic variations, larger samples sizes or longer readout times may be required to potentially ascertain statistical significance using these tools. Through this experiment, we demonstrated that FAST was able to detect tumor volume dynamics at hour-long time scales.

During this treatment session, we analyzed the impact of the mechanical stress placed on the sensor from the animal's movement, and we assessed the impact of the mechanical stress placed on the tumor by the sensor. Animals were able to freely move around, eat, and drink throughout the duration of the study when wearing the sensor. By the end of the study, neither the caliper measurements nor the bioluminescence imaging recorded a significant difference in tumor volume between mice with and without the sensor when receiving the same treatment (Fig. 2, G to L), suggesting that the sensor neither positively nor negatively affected the tumor volume progression or regression. For the drug-treated groups of mice, there was no statistically significant difference in tumor volume regression between the groups with and without sensors over the 6-day measurement period [calipers, $P = 0.24$; bioluminescence, $P = 0.84$; one-way analysis of variance (ANOVA) with Tukey's multiple comparisons test]. For the vehicle-treated mice, there was no statistically significant difference in tumor volume progression between the groups with and without sensors over the 6-day measurement period (calipers, $P = 0.94$; bioluminescence, $P = 0.97$; one-way ANOVA with Tukey's multiple comparisons test). We performed an analysis of the normal pressure exerted by the elastic sensor on the tumor, presented in the Supplementary Materials, and we noted that the pressure exerted by the sensor is approximately one order of magnitude less than the interstitial fluid pressure of a tumor (*25*). While the sensor backpack is made of a more rigid material that may stifle tumor growth, the backpack allows tumors to grow unencumbered to more than 17 mm in their greatest length, a traditional point of euthanasia. Overall, we saw no significant effects from sensor placement on tumor volume progression or regression.

Histological evidence supports the rapid sensor classification of responsive and nonresponsive tumors using FAST by demonstrating that the tumors undergo modifications at the cellular level within hours after treatment administration (Fig. 3). We compared histology samples from tumors undergoing the full erlotinib and vehicle treatment schedule with tumors excised 5 hours after erlotinib treatment initiation. Immunohistochemistry from tumors excised at the 5-hour time point showed an up-regulation of cleaved caspase 3, a marker for cell death. These same tumors also exhibited a down-regulation in Ki67, a marker strongly associated with cell proliferation. Moreover, these tumors presented a down-regulation of phosphorylated EGFR, which is a direct pharmacodynamic response to erlotinib. In addition to the immunohistochemistry performed in this study, previous studies examining the pharmacokinetics and pharmacodynamics of erlotinib demonstrate that biological effects from the drug begin occurring within 5 hours in humans, mice, and cell culture (*22*–*24*). Hematoxylin and eosin–stained histology from tumors undergoing the entire treatment schedule showed that erlotinib reduced the cell density in the tumor compared to vehicle-treated tumors. No difference is seen in the histology between tumors that underwent the sensor wrapping compared to tumors where the sensor was not administered. Hematoxylin and eosin–stained histology of skin where the sensors were placed for 1 week showed no signs of tissue damage. These results support the hypothesis that the sensor recorded tumor volume shrinkage in treated mice that directly related to drug pharmacodynamics and that the sensor wrapping did not affect the growth dynamics of the tumor.

To demonstrate that our sensor detected changes in tumor regression in multiple tumor models and treatment modalities, we also performed sensor characterization on an A20 B cell lymphoma solid tumor model in Balb/c mice using an experimental immunotherapy. Specifically, we treated the mice with an unmethylated cytosine-guanine (CG)-enriched oligodeoxynucleotide (CpG), a Toll-like receptor 9 (TLR9) ligand, and anti-OX40 antibody via intratumoral injections (*26*). The sensor measurements in this tumor model were only directly compared to caliper measurements because the presence of luminescence proteins in the cells generated an immune response that confounded the effects of the treatment. Similar to the last experimental model, the sensor was able to detect a change in tumor regression between drug- and vehicle-treated tumors within 5 hours after sensor placement. All drug-treated tumors had lower relative sensor readout than the vehicle-treated tumors (Fig. 4, A and B). Three weeks following therapy administration, every treated tumor was completely eradicated, comparable to the results published previously on this therapy and tumor model (*26*). Both the sensor and the caliper recorded significant tumor shrinkage in drug-treated tumors compared to vehicle-treated tumors over the entire treatment period (Fig. 4, C to F). The rapid reduction in tumor size may be a result of the CpG alone rather than an immune response triggered by the combination therapy; CpG has been shown to have rapid antitumor effects on its own, and immune cell infiltration may require longer time scales to take full effect (*26*). This study confirms that the sensor can determine tumor volume regression on multiple in vivo models and with multiple treatment modalities.

Immunohistochemistry from the A20 tumors demonstrates an immediate pharmacodynamic response following treatment initiation that supports the FAST measurement readouts. Specifically, the cell death marker cleaved caspase 3 was up-regulated in tumors

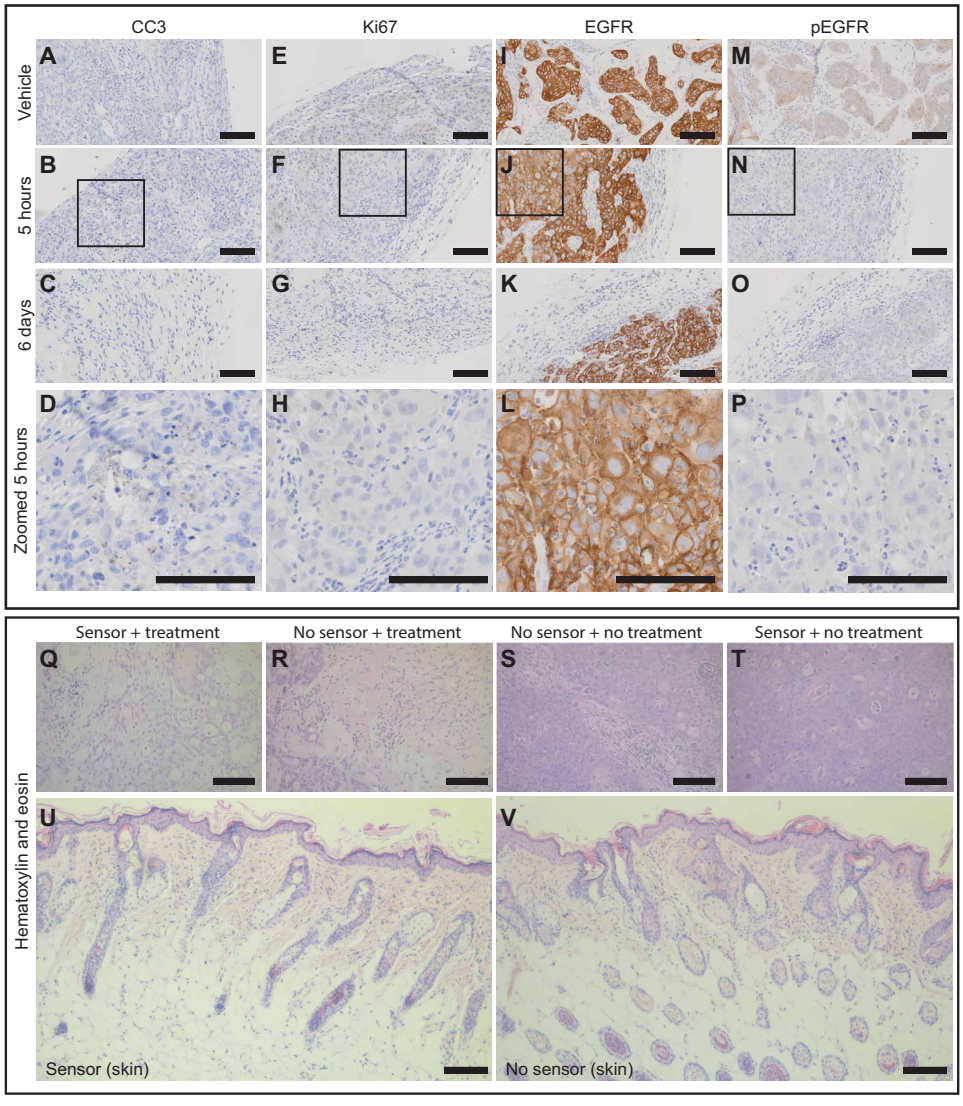

Fig. 3. Histology from HCC827 tumors treated with erlotinib validates rapid FAST sensor readouts of tumor volume regression. (**A** to **P**) Immunohistochemistry of tumors excised from mice treated for 6 days with vehicle (vehicle), treated for 5 hours with erlotinib, or treated for 6 days with erlotinib. Stains are for cleaved caspase 3 (CC3), a marker associated with cell death; Ki67, a marker associated with cell proliferation; EGFR; and phosphorylated EGFR (pEGFR). Erlotinib is an active inhibitor of EGFR and prevents phosphorylation. (**Q** to **V**) Hematoxylin and eosin stains of (Q and R) tumors and (U and V) skin from mice that did or did not wear FAST for 6 days. In the histological sampling, there is no noticeable difference in the cell shapes or distributions between the samples from mice wearing the sensor and the samples from mice not wearing the sensor. Scale bars, 100 μm.

within 6 hours after treatment initiation (Fig. 4, G and H), but the cell proliferation marker Ki67 was still present in the treated tumors at the 6-hour excision time point (Fig. 4, I and J). CpG also initiated an up-regulation of OX40 within 6 hours after initiation, providing a target for the dosed antibodies to bind to and stimulate an immune response (Fig. 4, K and L).

To ensure that measurement errors associated with mouse movements or the sensor itself did not affect the ability for FAST to discern growth or shrinkage in in vivo tumors, we compared sensor readouts from tumor-bearing mice with sensor readouts from mice without any tumors. We expected that measurements from sensors placed on mice without tumors would consistently fall in between the measurements taken from tumors that were expected to either shrink or grow. Over the first 12 hours after sensor placement, growing vehicle-treated tumors demonstrated a statistically significantly higher relative sensor readout compared to sensors that were placed on animals without any tumors. Similarly, CpG- and anti-OX40–treated shrinking tumors demonstrated a statistically significantly lower relative sensor readout compared to the same control group without tumors (fig. S6). This demonstrates that any errors associated with FAST sensor measurements do not affect the ability for FAST to discern tumor growth or shrinkage on the hour-long time scale.

DISCUSSION

Here, we presented a sensor system capable of autonomously, continuously, and accurately measuring subcutaneous solid tumor size regression. The FAST strain sensor has an initial resistance on the

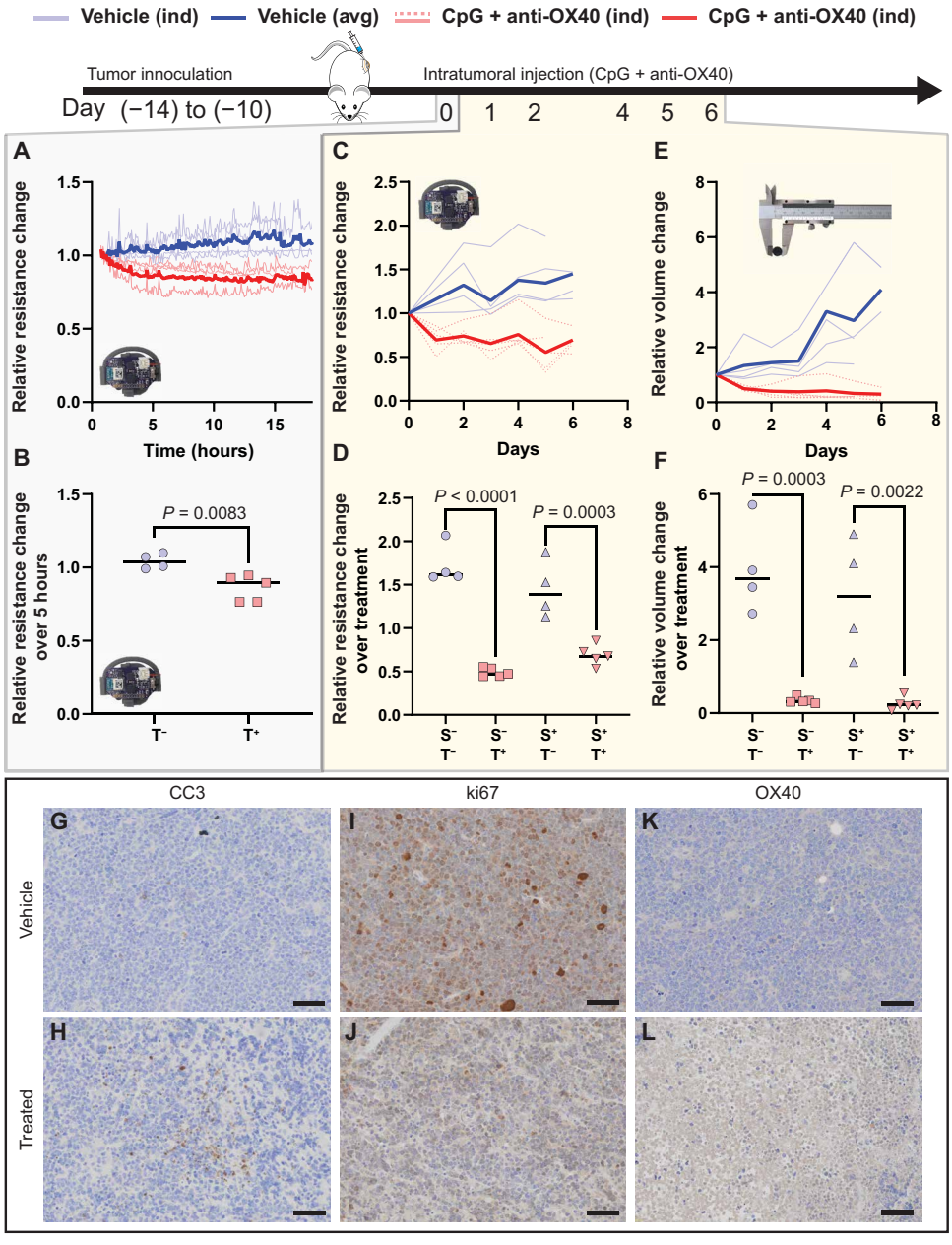

Fig. 4. FAST sensor detects a decrease in tumor volume sooner than existing methods in A20 mouse models treated intratumorally with CpG + anti-OX40. (**A** to **D**) FAST reads out tumor volume progression or regression continuously at 5-min intervals in Balb/c mice with subcutaneous A20 B cell lymphoma tumors receiving 40 μg of CpG and 4 μg of anti-OX40 ($n = 5$) or vehicle ($n = 4$) treatments over (A and B) the first few hours following treatment or (C and D) the entire treatment period in the same mice. Individual mouse sensor trend lines are presented as seven-point moving averages. (**E** and **F**) Tumor volume measurements using calipers confirm FAST readouts over the entire treatment period. (**G** to **L**) Immunohistochemistry of tumors excised from mice treated for 6 days with vehicle (vehicle) or treated once with CpG + anti-OX40 (treated). Staining is against (G and H) CC3, (I and J) Ki67, and (K and L) OX40. The treated stains are from tumors excised within 6 hours after treatment initiation. T^+, CpG and anti-OX40 treatment; T^-, vehicle treatment; S^+, with FAST sensor; S^-, no FAST sensor. Scale bars, 50 μm. Data are presented as individual data point or curves. Bold line, average; (B) unpaired two-tailed Student's *t* test; (D and F) one-way ANOVA with Tukey's multiple comparisons test.

order of 100 ohms, increases up to 100 times that value from 0 to 75% strain, is sensitive to 0.1% (10-μm) changes in strain, and can measure dynamic volume changes in ellipsoids with sizes ranging from 65 to 750 mm^3. We demonstrated that the sensor's high resolution in both time and space enables the ability to discern initial treatment efficacy within just 5 hours after therapy initiation in two preclinical subcutaneous tumor models, and the sensor can read out continuously for >24 hours on a single battery charge. Each reusable sensor backpack costs ~$60 to fabricate, can be scaled for mass manufacturing, and takes <5 min of low-skill work to apply to an animal. Over weeklong treatment periods, sensor readout dynamics closely correlated with caliper and bioluminescent imaging measurement dynamics; however, because the sensor measures the tumor differently, via resistance variations correlating with

changing circumferences rather than diameter or luminescence measurements, each measurement tool cannot directly convert its measurements to that of another. For example, while the sensor is sensitive to all characteristic dimensions of the tumor, it is slightly more sensitive to tumor height changes because of the geometric transformations that the tumor and sensor undergo.

Our sensor focuses on measuring short-term primary tumor regression rather than metastatic progression or regression. For metastatic models, our sensor could provide a dataset that rapidly categorizes ineffective treatments by accurately capturing primary tumor growth. For potentially effective treatments in which FAST sensors rapidly read out a reduction in the primary tumor's volume, however, the sensor data could be used as an indicator to perform follow-up screenings that provide additional information on tumor regression that confirm a reduction in total tumor burden. Notably, some tumors are known to undergo pseudoprogression after treatment initiation, a phenomenon where the tumor grows for a period of time preceding subsequent regression, and the occurrence of tumor growth does not necessarily signify a failed therapy (*27*, *28*). In our studies, we directly compared the tumor regression of vehicle- and drug-treated mice, providing appropriate controls to ensure confidence in our measurements. While our sensors did not detect tumor pseudoprogression during the treatments, future work may enable us to detect differences between normal progression and pseudoprogression growth rates using the real-time data generated by our sensor. Moreover, because our sensor can be worn continuously, it has the ability to read out treatment regimens for longer periods of time than presented here and can still be used to categorize the effectiveness on tumors undergoing a short period of pseudoprogression.

Notably, while we developed an encapsulated version of the sensor that can withstand contact with fluid (fig. S7), the size limitations of a mouse model prevent the implantation of FAST due to the volume of the PCB and battery. For this reason, the implantable version of this sensor was not tested in vivo during our experiments, and we limited our experiments to testing on subcutaneous tumors. Further work optimizing the battery life and size of the associated electronic PCB is required in pursuit of a longer-lasting and implantable sensor system. Passive wireless sensing systems may provide an alternative path to the implementation of implantable sensor systems (*29*–*31*), and other implantable strain sensors have passed wires through the skin (*32*) or used imaging techniques to visualize the strain sensor within the body (*33*) to avoid the implantation of the PCB. However, these methods reduce the readout sensitivity or biocompatibility of the systems. Because the sensor can detect tumor volume changes associated with treatments in real time, it could potentially be combined with drug delivery systems to enable a theranostic closed-loop delivery platform; however, additional studies will be required to understand the efficacy of such a proposed system. Moreover, utilization of the sensor requires singly housing mice to mitigate the risk of damage to the wiring, which could potentially act as a throughput limitation. There exists some variability between the exact resistance readouts of different sensors at given strains, but preliminary testing in vitro enables calibration between sensors and provides a consistency check before moving to in vivo testing. This sensor is designed specifically for preclinical drug screening trials, and any efforts to translate the sensor to humans should consider the surgical impact associated with placing the sensor at a given tumor location. Regardless of these limitations, this sensor's ability to continuously, autonomously, and accurately record tumor volume regression suggests that this method could supplant current tumor regression measurement techniques used during in vivo preclinical trials, unlocking new avenues for high-throughput in vivo drug discovery screenings and basic cancer research that takes advantage of the sensor's time-dependent datasets.

MATERIALS AND METHODS

Sensor backpack fabrication

A schematic of the sensor and its fabrication process is found in fig. S1. Sensors were fabricated on a 5.0 cm–by–7.5 cm glass slide (Fisher Scientific, Waltham, USA). As an anti-stick coating, a Micro-90 solution (Cole-Parmer, Vernon Hills, USA) was coated on a slide by spin-coating 300 μl of solution on the slide at 600 rpm for 20 s. A WS-650MZ-23NPP spin-coater from Laurell Technologies (North Wales, USA) was used. Solutions of SEBS (33 and 50 mg/ml; Asahi Kasei, 1221, Chiyoda City, Japan) in cyclohexane (Fisher Scientific) were generated, and the solution was mixed overnight. The SEBS solution was then drop-casted on a 3 inch–by–2 inch glass slide. To create the 28-μm-thick substrate, 4 ml of solution at 33 mg/ml was used. To create the 41-μm-thick substrate, 4 ml of solution at 50 mg/ml was used. To create the 72-μm-thick substrate, 4 ml of solution at 50 mg/ml and 2 ml of solution at 33 mg/ml were combined and used. A transparency film (ACCO Brands, Boonville, USA) mask was mechanically cut using a Cricut machine (South Jordan, USA) from a mask designed in SolidWorks (Dassault Systèmes, Vélizy-Villacoublay, France). The sensor design consisted of an 11 mm–by–1.5 mm strip, book ended by 3 mm–by–3 mm connection pads. Once cut, the transparency film was sprayed with a nonstick Teflon spray (DuPont, Eleutherian Mills, USA) and placed on the SEBS substrate. Then, a 50-nm layer of gold was deposited on the SEBS at 0.6 Å/s using a metal evaporator from Thermionics Laboratory Inc. (Hayward, USA). Gallium-indium eutectic (Sigma-Aldrich, St. Louis, USA) was placed on the connection pads, and a 30-gauge multicore wire (McMaster-Carr, Elmhurst, USA) was attached to the connection pad using paper tape. The wires were then soldered to a custom-designed PCB (see fig. S3) assembled by Digicom Electronics (Oakland, USA). The circuit board is powered by a 150-mA·hour lithium-ion rechargeable battery (Digi-Key, Thief River Falls, USA). When awake, the average current draw for the circuit board is 3.5 mA. The sensor backpack (see fig. S1) was printed in three pieces on a Formlabs Form 2 printer (Somerville, USA). The two rigid rods were printed in either rigid resin or gray resin, while the flexible base was printed in flexible resin.

Gold was chosen as an electrically conductive layer over carbon nanotubes and silver nanowires, which have also been demonstrated to work as strain sensors, because of its well-studied biocompatibility and lower hysteresis compared to the other materials. SEBS 1221 was chosen as a substrate for three reasons: (i) its ability to have gold readily stick to it without a chromium layer, enabling better adhesion properties during repeated stretching; (ii) its soft mechanical properties provided less stress on the tumor compared to other polymers; and (iii) unlike polydimethylsiloxane (PDMS), SEBS does not propagate cracks as easily, providing a sensor that is more resistant to animal interaction.

Fully encapsulated sensors were fabricated by first spin-coating a PDMS (SYLGARD 184, Dow, Midland, USA) layer mixed at a 10:1 ratio (PDMS:cross-linker) at 1000 rpm for 30 s. The PDMS was

then cured at 70°C for 12 hours. Then, a 40-nm-thick gold film was evaporated onto the PDMS substrate at 0.5 A/s. This gold film was sandwiched between two 3-nm-thick evaporated chromium films and patterned using the transparency shadow masks described above. Gallium-indium eutectic (Sigma-Aldrich) was placed on the sensor connection pads along with a 36-gauge multicore wire (McMaster-Carr). The entire device was then fully encapsulated in Kwik-Sil (World Precision Instruments, Sarasota, USA). We demonstrated that the device could remain in contact with phosphate-buffered saline and with mouse tissue in euthanized mice while maintaining its conductivity and ability to read out strain measurements through changes in resistance between 0 and 40% strain. When in contact with mouse tissue, the devices were fully wrapped around the tissue of interest to create a loop, and the two sides of the sensor loop were fixed together using Kwik-Sil. The wires were then passed through the skin of the tissue out to the battery and PCB. Because of the requirement for a nondegradable battery and PCB to read out the device, these materials were designed to be biocompatible but not biodegradable. The lack of biodegradable parts potentially enables the ability to perform long-term measurements with the sensor that tracks tumor progression and regression over weeks-long treatment periods.

While stretchable sensors are known to undergo hysteresis and experience drift during repeated cycling, the fact that this application of the sensor only requires one stretching cycle eliminates the potential for error associated with these material-based concerns. Moreover, the viscoelastic properties of SEBS cause the sensor to experience a reduction in resistance over time (fig. S2B), but the sensor approaches equilibrium approximately 30 min after strain is applied. For this reason, in vivo measurements were normalized to the data points taken 30 min or more after sensor placement. Placing the sensors on a 3D object compared to providing strain in 1D may affect the exact readouts of the sensor; however, the data in Fig. 1G demonstrate that an increase in resistance is still exponentially proportional to an increase in the ellipsoid shape that the sensor is wrapped around. Last, animal movement does cause the sensor to constantly undergo small changes in strain; however, these small changes in strain are averaged out over multiple points and have been shown through our measurements to not affect the statistical significance of the in vivo experiments (fig. S6).

Sensor in vitro characterization

To measure the resistance during stretching, we attached samples to a homemade stretching station and connected the samples to an LCR meter (Keysight Technologies, E4980, Santa Rosa, USA). Before beginning the measurements, sensors were stretched to 200% strain by hand more than 20 times. Samples were then stretched between 0 and 100% strain at 1% intervals, approximately 120 μm per step, and resistance measurements were recorded in LabVIEW (National Instruments, Austin, USA). Following this test, the samples were then stretched to 50% strain, and the resistance of the sensor was measured over the course of 45 min. This test demonstrated that although the sensor underwent relaxation over time, much of the relaxation occurred within the first 45 min (see fig. S1). After this test, the sensor was then stretched from 50 to 60% strain at 0.083% intervals, approximately 10 μm per step.

To measure the force required to strain the sensor to a given length, we attached the samples to an Instron 5565 (Norwood, USA). We stretched the samples at a rate of 50 mm/min, zeroing the displacement and the force once the sample reached 0.05-N force. Forces were recorded using a 100-N force gauge provided by Instron and read out on the machine's accompanying software. Each sample was stretched until its breaking point.

To measure the thickness of each sensor, we used a Bruker DektakXT-A profilometer (Billerica, USA) and took the average of 10 different readings from multiple sensors taken from various locations on the sensor. The edges of the sensor tended to have a slightly thicker measurement compared to the center of the sensor, leading to a slight variability in thickness readouts (see fig. S1).

To measure the ability of FAST to read out the variation in volume of different shapes, we 3D printed ellipsoid shapes cut in half down their center line. All shapes were scaled linearly and had heights between 2.5 and 5.6 mm, as measured using calipers. These shapes were designed in SolidWorks and printed on an Ultimaker 3 using Ultimaker PLA filament (Geldermalsen, Netherlands). The FAST devices were placed on the shapes, and the sensors were allowed to relax for 20 s before the resistance measurement was recorded.

Subcutaneous HCC827 tumor treatment with erlotinib

All animal procedures were approved by the Stanford Institutional Animal Care and Use Committee and conducted in accordance with Stanford University animal facility guidelines. The HCC827 human lung cancer cell line was obtained from the American Type Culture Collection (ATCC; CRL-2868; Manassas, USA) and was then transfected with the firefly luciferase reporter gene. Before injecting the cells into mice, the cells were tested and shown to be pathogen-free by the Stanford Department of Comparative Medicine Veterinary Service Center (Stanford, USA). Five million cells were injected into the right flank of six- to eight-week-old Nu/Nu mice (Charles River Laboratories, Wilmington, USA) after being mixed with Matrigel (Corning, Corning, USA). Mice were housed in the Laboratory Animal Facility of the Stanford University Medical Center (Stanford, CA).

The sensors were placed on six of the animals once the tumors reached a size of approximately 100 mm^3 and were left on the animals for 1 day. When placing the sensors on the animals, the mice were anesthetized with 1 to 3% isoflurane. Buprenorphine sustained release was also dosed to the animals at 0.5 to 1.0 mg/kg. Before beginning the procedure, we checked the absence of paw reflexes by pinching a hind paw with tweezers and checked the absence of eye reflexes to make sure that the animal was fully anesthetized. A protective eye liquid gel (GenTeal, Alcon, Geneva, Switzerland) was then applied to the eyes with a cotton-tipped swab. If necessary, we then shaved the location where the sensor was to be attached to the animal around the tumor. The skin was then aseptically prepared with alternating cycles of Betadine or a similar scrub and 70% ethyl alcohol. Using a surgical tissue glue (3M, Saint Paul, USA), the sensor was attached to the skin of the animal so that the tumor was positioned in the center of the sensor. A 1.3-inch-diameter Tegaderm wrap was then applied on top of the sensor and to the animal's skin so that the sensor remained snuggly attached to the animal. The battery was similarly attached to the skin using Tegaderm and was placed on the opposite flank of the sensor. Every day that the sensor remained on the animal, the battery was replaced and the Tegaderm wrap was replaced above the battery.

Once the tumor reached a volume of approximately 200 mm^3, the mice were broken up into four groups of six: One group received the erlotinib treatment and the sensor protocol. One group received the erlotinib treatment and did not receive the sensor protocol. One

group received a vehicle treatment and did receive the sensor protocol, and one group received a vehicle treatment and did not receive the senor protocol. The treated mice were dosed with erlotinib hydrochloride (Fisher Scientific) dissolved in a mixture of Captisol (Selleckchem, Houston, USA) and water. Erlotinib was dosed at 50 mg/kg via an oral gavage to mice. Mice that did not receive the erlotinib were dosed with vehicle only. Dosing occurred on days 0, 1, 2, 4, and 5. On day 3, mice did not receive treatment, and they also did not receive the sensor protocol. DietGel 76A and sterile water gel (ClearH$_2$0, Westbrook, USA) were placed in the mouse cages to ensure easy access to food and hydration. The weight of each mouse was recorded over time, and these data are presented in fig. S8. Mice wearing the sensor were singly housed to prevent other mice from chewing through the sensor backpack. On days 0, 3, and 6, all mice underwent caliper measurements (McMaster-Carr), individual time-point sensor measurement, and bioluminescence imaging. Luminescence imaging was performed on a Lago X (Spectral Instruments Imaging, Tucson, USA), and image analysis was performed in the accompanying Aura software. In this experiment, we used the 28-μm-thick sensors presented here; however, we found that during our testing, 9 of 24 sensors lost their electrical connection, likely because of kinetic friction causing the gold layer to shed from the SEBS. In the subsequent in vivo experiment with the A20 tumor model, the 41-μm-thick sensors were used, and all sensors performed unceasingly over the entire period of interest without any failures. Only sensors that recorded data are presented in Fig. 2, and no other data were removed from the analysis. The mice were euthanized on day 6, and the tumors and skin next to the sensors were harvested for histology.

The excised tissues were fixed in a 4% paraformaldehyde solution for more than 24 hours, followed by 70% ethanol for more than 24 hours. Immunohistochemistry staining used the following antibodies: EGFR (D38B1) XP Rabbit mAb (#4267, Cell Signaling Technology, Danvers, USA), Phospho-EGFR (Tyr^{1068}) (D7A5) XP Rabbit mAb (#3777, Cell Signaling Technology), Cleaved Caspase-3 (Asp^{175}) (D3E9) Rabbit mAb (#9579, Cell Signaling Technology), Ki67 Polyclonal Antibody (#27309-1-AP, Proteintech Group, Rosemont, USA), and Biotinylated Goat Anti-Rabbit IgG (H+L) (ab64256, Abcam, Cambridge, UK). Horseradish peroxidase–conjugated streptavidin was purchased from Thermo Fisher Scientific. DAB Substrate Kit ab64238 was purchased from Abcam. Antigen retrieval was performed by incubation for 20 min in citric acid (pH 6.0) at 100°C. Antibody dilutions and staining procedures were performed as suggested by the manufacturer.

Subcutaneous A20 tumor treatment with CpG and anti-OX40

All animal procedures were approved by the Stanford Institutional Animal Care and Use Committee and conducted in accordance with Stanford University animal facility guidelines. The A20 B cell lymphoma cell line was obtained from the ATCC (TIB-208). Before injecting the cells into mice, the cells were tested and shown to be pathogen-free by the Stanford Department of Comparative Medicine Veterinary Service Center (Stanford, USA). Five million cells were injected into the right flank of six- to eight-week-old Balb/c mice (Charles River Laboratories, Wilmington, USA). Mice were housed in the Laboratory Animal Facility of the Stanford University Medical Center (Stanford, CA). As described in the "Subcutaneous HCC827 tumor treatment with erlotinib" section, mice were split into treatment and vehicle groups, and the sensors were applied to all the animals. Caliper measurements and sensor measurements were recorded daily over the span of 6 days. In this model, we used sensors with a 41-μm-thick layer of SEBS, and all sensors performed unceasingly over the entire period of interest. On days 0, 1, 2, 4, 5, and 6, the treated animals were injected with 40 μg of CpG ODN 2395 (InvivoGen, San Diego, USA), a class C tlr9 ligand, and 4 μg of anti-OX40 (CD134) mAb (rat IgG1, clone OX86; Bio X Cell, Lebanon, USA). The total volume injected in the drug- and vehicle-treated mice was ~13 to 16 μl and varied depending on the concentration of the antibody. The weight of each mouse was recorded over time, and these data are presented in fig. S8. On day 3, the sensor was removed from the animal, and no therapy was given to the animal. Figure S9 also includes data showing the tumor progression or regression of drug- and vehicle-treated mice that did not continuously wear the FAST sensor. DietGel 76A and sterile water gel (ClearH$_2$O, Westbrook, USA) were placed in the mouse cages to ensure easy access to food and hydration. Mice wearing the sensor were singly housed to prevent other mice from chewing through the sensor backpack.

Tumor compression experiments

Using an Instron machine, two steel compression platens compressed an excised tumor at 2 mm/min. Excised tumors were tested on the machine within 1 hour following euthanasia, and the tumors were kept in phosphate-buffered saline after excision and before testing. Both vehicle- and drug-treated A20 tumors were dosed via an intratumoral injection 1 day before tumor excision. The force-versus-displacement readouts were recorded on the accompanying Instron software and are presented in fig. S10. Notably, the software began recording once the force gauge read out a value of at least 3 mN.

Statistical analysis

No data were excluded from the analysis. Paired and unpaired two-tailed Student's *t* tests and one-way ANOVA tests with Tukey's multiple comparisons tests were performed using Prism version 8.3 (GraphPad) or Microsoft Excel (Microsoft). Paired *t* tests were used when performing direct comparisons between individual sensors at different strains. Unpaired *t* tests were used in other situations in which a paired *t* test was not appropriate. A $P < 0.05$ was considered statistically significant. Figure captions and text describe the number of replicates used in each study. Figure captions define the center line and error bars present in the plots. Before beginning our studies, we used historical data (*22*, *26*) on the chosen treatment models to determine whether we needed a sample size of at least three mice when comparing two experimental subgroups (sensor + treatment versus sensor + no treatment) and a sample size of at least six mice when comparing four experimental subgroups (sensor + treatment versus sensor + no treatment versus no sensor + no treatment versus no sensor + treatment) to achieve statistically significant results.

SUPPLEMENTARY MATERIALS

Supplementary material for this article is available at https://science.org/doi/10.1126/sciadv.abn6550

View/request a protocol for this paper from *Bio-protocol*.

REFERENCES AND NOTES

1. J. Drost, H. Clevers, Organoids in cancer research. *Nat. Rev. Cancer* **18**, 407–418 (2018).
2. G. Vlachogiannis, S. Hedayat, A. Vatsiou, Y. Jamin, J. Fernández-Mateos, K. Khan, A. Lampis, K. Eason, I. Huntingford, R. Burke, M. Rata, D.-M. Koh, N. Tunariu, D. Collins, S. Hulkki-Wilson, C. Ragulan, I. Spiteri, S. Y. Moorcraft, I. Chau, S. Rao, D. Watkins, N. Fotiadis, M. Bali, M. Darvish-Damavandi, H. Lote, Z. Eltahir, E. C. Smyth, R. Begum,

P. A. Clarke, J. C. Hahne, M. Dowsett, J. de Bono, P. Workman, A. Sadanandam, M. Fassan, O. J. Sansom, S. Eccles, N. Starling, C. Braconi, A. Sottoriva, S. P. Robinson, D. Cunningham, N. Valeri, Patient-derived organoids model treatment response of metastatic gastrointestinal cancers. *Science* **359**, 920–926 (2018).
3. M. A. Clarke, J. Fisher, Executable cancer models: Successes and challenges. *Nat. Rev. Cancer* **20**, 343–354 (2020).
4. B. Lim, Y. Lin, N. Navin, Advancing cancer research and medicine with single-cell genomics. *Cancer Cell* **37**, 456–470 (2020).
5. H. Gao, J. M. Korn, S. Ferretti, J. E. Monahan, Y. Wang, M. Singh, C. Zhang, C. Schnell, G. Yang, Y. Zhang, O. A. Balbin, S. Barbe, H. Cai, F. Casey, S. Chatterjee, D. Y. Chiang, S. Chuai, S. M. Cogan, S. D. Collins, E. Dammassa, N. Ebel, M. Embry, J. Green, A. Kauffmann, C. Kowal, R. J. Leary, J. Lehar, Y. Liang, A. Loo, E. Lorenzana, E. R. McDonald, M. E. McLaughlin, J. Merkin, R. Meyer, T. L. Naylor, M. Patawaran, A. Reddy, C. Röelli, D. A. Ruddy, F. Salangsang, F. Santacroce, A. P. Singh, Y. Tang, W. Tinetto, S. Tobler, R. Velazquez, K. Venkatesan, F. Von Arx, H. Q. Wang, Z. Wang, M. Wiesmann, D. Wyss, F. Xu, H. Bitter, P. Atadja, E. Lees, F. Hofmann, E. Li, N. Keen, R. Cozens, M. R. Jensen, N. K. Pryer, J. A. Williams, W. R. Sellers, High-throughput screening using patient-derived tumor xenografts to predict clinical trial drug response. *Nat. Med.* **21**, 1318–1325 (2015).
6. J. Ortmann, L. Rampášek, E. Tai, A. S. Mer, R. Shi, E. L. Stewart, C. Mascaux, A. Fares, N.-A. Pham, G. Beri, C. Eeles, D. Tkachuk, C. Ho, S. Sakashita, J. Weiss, X. Jiang, G. Liu, D. W. Cescon, C. A. O'Brien, S. Guo, M.-S. Tsao, B. Haibe-Kains, A. Goldenberg, Assessing therapy response in patient-derived xenografts. *Sci. Transl. Med.* **13**, eabf4969 (2021).
7. S. Xu, A. Jayaraman, J. A. Rogers, Skin sensors are the future of health care. *Nature* **571**, 319–321 (2019).
8. J. C. Yang, J. Mun, S. Y. Kwon, S. Park, Z. Bao, S. Park, Electronic skin: Recent progress and future prospects for skin-attachable devices for health monitoring, robotics, and prosthetics. *Adv. Mater.* **31**, 1904765 (2019).
9. J. Kim, A. S. Campbell, B. E. F. de Ávila, J. Wang, Wearable biosensors for healthcare monitoring. *Nat. Biotechnol.* **37**, 389–406 (2019).
10. T. Adrega, S. P. Lacour, Stretchable gold conductors embedded in PDMS and patterned by photolithography: Fabrication and electromechanical characterization. *J. Micromechanics Microengineering.* **20**, 055025 (2010).
11. I. R. Minev, P. Musienko, A. Hirsch, Q. Barraud, N. Wenger, E. M. Moraud, J. Gandar, M. Capogrosso, T. Milekovic, L. Asboth, R. F. Torres, N. Vachicouras, Q. Liu, N. Pavlova, S. Duis, A. Larmagnac, J. Vörös, S. Micera, Z. Suo, G. Courtine, S. P. Lacour, Electronic dura mater for long-term multimodal neural interfaces. *Science* **347**, 159–163 (2015).
12. S. P. Lacour, D. Chan, S. Wagner, T. Li, Z. Suo, Mechanisms of reversible stretchability of thin metal films on elastomeric substrates. *Appl. Phys. Lett.* **88**, 204103 (2006).
13. J. P. Wisnivesky, A. I. Mushlin, N. Sicherman, C. Henschke, The cost-effectiveness of low-dose CT screening for lung cancer: Preliminary results of baseline screening. *Chest* **124**, 614–621 (2003).
14. J. L. Sottnik, J. Dai, H. Zhang, B. Campbell, E. T. Keller, Tumor-induced pressure in the bone microenvironment causes osteocytes to promote the growth of prostate cancer bone metastases. *Cancer Res.* **75**, 2151–2158 (2015).
15. C. I. Henschke, D. F. Yankelevitz, R. Yip, V. Archer, G. Zahlmann, K. Krishnan, B. Helba, R. Avila, Tumor volume measurement error using computed tomography imaging in a phase II clinical trial in lung cancer. *J. Med. Imaging.* **3**, 035505 (2016).
16. G. D. Ayers, E. T. McKinley, P. Zhao, J. M. Fritz, R. E. Metry, B. C. Deal, K. M. Adlerz, R. J. Coffey, H. C. Manning, Volume of preclinical xenograft tumors is more accurately assessed by ultrasound imaging than manual caliper measurements. *J. Ultrasound Med.* **29**, 891–901 (2010).
17. M. M. Jensen, J. T. Jørgensen, T. Binderup, A. Kjær, Tumor volume in subcutaneous mouse xenografts measured by microCT is more accurate and reproducible than determined by 18F-FDG-microPET or external caliper. *BMC Med. Imaging* **8**, 16 (2008).
18. S. Mollard, R. Fanciullino, S. Giacometti, C. Serdjebi, S. Benzekry, J. Ciccolini, In vivo bioluminescence tomography for monitoring breast tumor growth and metastatic spreading: Comparative study and mathematical modeling. *Sci. Rep.* **6**, 1–10 (2016).
19. O. Jonas, H. M. Landry, J. E. Fuller, J. T. Santini, J. Baselga, R. I. Tepper, M. J. Cima, R. Langer, An implantable microdevice to perform high-throughput in vivo drug sensitivity testing in tumors. *Sci. Transl. Med.* **7**, 284ra57 (2015).
20. C. Dagdeviren, Y. Shi, P. Joe, R. Ghaffari, G. Balooch, K. Usgaonkar, O. Gur, P. L. Tran, J. R. Crosby, M. Meyer, Y. Su, R. C. Webb, A. S. Tedesco, M. J. Slepian, Y. Huang, J. A. Rogers, Conformal piezoelectric systems for clinical and experimental characterization of soft tissue biomechanics. *Nat. Mater.* **14**, 728–736 (2015).
21. E. Song, Z. Xie, W. Bai, H. Luan, B. Ji, X. Ning, Y. Xia, J. M. Baek, Y. Lee, R. Avila, H. Y. Chen, J. H. Kim, S. Madhvapathy, K. Yao, D. Li, J. Zhou, M. Han, S. M. Won, X. Zhang, D. J. Myers, Y. Mei, X. Guo, S. Xu, J. K. Chang, X. Yu, Y. Huang, J. A. Rogers, Miniaturized electromechanical devices for the characterization of the biomechanics of deep tissue. *Nat. Biomed. Eng.* **5**, 759–771 (2021).
22. J. Schöttle, S. Chatterjee, C. Volz, M. Siobal, A. Florin, D. Rokitta, Y. Hinze, F. Dietlein, D. Plenker, K. König, K. Albus, J. M. Heuckmann, D. Rauh, T. Franz, B. Neumaier, U. Fuhr, L. C. Heukamp, R. T. Ullrich, Intermittent high-dose treatment with erlotinib enhances therapeutic efficacy in EGFR-mutant lung cancer. *Oncotarget* **6**, 38458–38468 (2015).
23. S. R. Christiansen, A. Broniscer, J. C. Panetta, C. F. Stewart, Pharmacokinetics of erlotinib for the treatment of high-grade glioma in a pediatric patient with cystic fibrosis: Case report and review of the literature. *Pharmacotherapy* **29**, 858–866 (2009).
24. Q. Wu, M. Y. Li, H. Q. Li, C. H. Deng, L. Li, T. Y. Zhou, W. Lu, Pharmacokinetic-pharmacodynamic modeling of the anticancer effect of erlotinib in a human non-small cell lung cancer xenograft mouse model. *Acta Pharmacol. Sin.* **34**, 1427–1436 (2013).
25. S. Goel, D. G. Duda, L. Xu, L. L. Munn, Y. Boucher, D. Fukumura, R. K. Jain, Normalization of the vasculature for treatment of cancer and other diseases. *Physiol. Rev.* **91**, 1071–1121 (2011).
26. I. Sagiv-Barfi, D. K. Czerwinski, S. Levy, I. S. Alam, A. T. Mayer, S. S. Gambhir, R. Levy, Eradication of spontaneous malignancy by local immunotherapy. *Sci. Transl. Med.* **10**, eaan4488 (2018).
27. V. L. Chiou, M. Burotto, Pseudoprogression and immune-related response in solid tumors. *J. Clin. Oncol.* **33**, 3541–3543 (2015).
28. V. Kurra, R. J. Sullivan, J. F. Gainor, F. S. Hodi, L. Gandhi, C. A. Sadow, G. J. Harris, K. Flaherty, S. Lee, Pseudoprogression in cancer immunotherapy: Rates, time course and patient outcomes. *J. Clin. Oncol.* **34**, 6580 (2016).
29. S. Niu, N. Matsuhisa, L. Beker, J. Li, S. Wang, J. Wang, Y. Jiang, X. Yan, Y. Yun, W. Burnett, A. S. Y. Poon, J. B. H. Tok, X. Chen, Z. Bao, A wireless body area sensor network based on stretchable passive tags. *Nat. Electron.* **2**, 361–368 (2019).
30. L. Y. Chen, B. C.-K. Tee, A. L. Chortos, G. Schwartz, V. Tse, D. J. Lipomi, H.-S. P. Wong, M. V. McConnell, Z. Bao, Continuous wireless pressure monitoring and mapping with ultra-small passive sensors for health monitoring and critical care. *Nat. Commun.* **5**, 1–10 (2014).
31. H. Jiang, N. M. Carter, A. Zareei, S. Nejati, J. F. Waimin, S. Chittiboyina, E. E. Niedert, T. Soleimani, S. A. Lelièvre, C. J. Goergen, R. Rahimi, A wireless implantable strain sensing scheme using ultrasound imaging of highly stretchable zinc oxide/poly dimethylacrylamide nanocomposite hydrogel. *ACS Appl. Bio Mater.* **3**, 4012–4024 (2020).
32. P. Mostafalu, M. Akbari, K. A. Alberti, Q. Xu, A. Khademhosseini, S. R. Sonkusale, A toolkit of thread-based microfluidics, sensors, and electronics for 3D tissue embedding for medical diagnostics. *Microsystems Nanoeng.* **2**, 1–10 (2016).
33. J. Lee, S. J. Ihle, G. S. Pellegrino, H. Kim, J. Yea, C. Y. Jeon, H. C. Son, C. Jin, D. Eberli, F. Schmid, B. L. Zambrano, A. F. Renz, C. Forró, H. Choi, K. I. Jang, R. Küng, J. Vörös, Stretchable and suturable fibre sensors for wireless monitoring of connective tissue strain. *Nat. Electron.* **4**, 291–301 (2021).

Acknowledgments: We thank members of the Bao, Gambhir, and Hiesinger laboratories for helpful discussions on the project. We thank I. Alam for advice about cell culture and the A20 tumor model. We thank B. Murmann and N. Vitale for contributions to the design of the PCB. We acknowledge the Stanford Center for Innovation in In vivo Imaging (SCi^3) small animal imaging center and the Stanford Animal Histology Services for supporting the imaging and histology performed here. We acknowledge the Stanford Veterinary Services and M. Huss for help in designing the animal experiments. Part of this work was performed at the Stanford Nano Shared Facilities, supported by the NSF under award ECCS-1542152. The photo of the hand with the cell phone in Fig. 1 is provided with the permission of Facebook Design Resources (license: https://design.facebook.com/license/). The photo of the calipers in Figs. 2 and 4 was distributed by Wikimedia Commons under a Creative Commons 3.0 license and was taken by S. Eugster. **Funding:** A.A. acknowledges funding from an NIH F32 fellowship (grant 1F32EB029787) and the Stanford Wearable Electronics Initiative (eWEAR). **Author contributions:** A.A., P.M., S.S.G., and Z.B. designed the project and experiments. A.A. and N.M. designed the strain sensor. A.A. designed the sensor backpack device. A.A. and A.M.-B. performed in vitro characterization of the sensors. A.A. and Y.K. designed the PCB and cell phone app. C.T.C., R.F., and R.S. performed cell culture. A.A. and C.T.C. performed the animal experiments. A.A., and Z.B. wrote the manuscript. All authors reviewed and commented on the manuscript. **Competing interests:** A.A. and Z.B. are inventors on a provisional patent related to this work filed by Board of Trustees of the Leland Stanford Junior University (no. 63/230,428, filed 6 August 2021). The authors declare that they have no other competing interests. **Data and materials availability:** All data needed to evaluate the conclusions in the paper are present in the paper and/or the Supplementary Materials.

Submitted 10 December 2021
Accepted 12 July 2022
Published 16 September 2022
10.1126/sciadv.abn6550